ARTICLE https://doi.org/10.53480/4e7a-4y94

PLANETARY RESEARCH

Geology of Atlas crater, the prime landing site of the Emirates Lunar Mission Rashid-1 rover

Jessica Flahaut [1], **Christian Wöhler** [2], **Marine Joulaud** [1,3], **Evelyn Füri** [1], **Megha Bhatt** [4], **Sylvain Breton** [1], **Sebastian G. Els** [5], **Sara AlMaeeni** [5], **Hamad AlMarzooqi** [5], **the ELM Science Collaboration** [1]

[1]Université de Lorraine, CNRS, CRPG, 54000 Nancy, France

[2]Image Analysis Group, TU Dortmund University, Otto-Hahn-Str. 4, 44227 Dortmund, Germany

[3]Laboratoire de Géologie de Lyon : Terre, Planètes, Environnement (LGL-TPE), Université Claude Bernard Lyon1/CNRS/ENS, 69622 Villeurbanne, France

[4]Physical Research Laboratory, Ahmedabad 380009, India

[5]Mohammed Bin Rashid Space Centre (MBRSC), PO Box 211833, Dubai, United Arab Emirates

Corresponding author
(jessica.flahaut@univ-lorraine.fr)

Received
February 20, 2026
Accepted
May 18, 2026
Published
August 27, 2026

Handling Editor
Caitlin Ahrens, NASA Goddard Space Flight Center, University of Maryland, College Park, USA

The peer review report of this article is available on the journal website.

Article summary

The present paper describes the complex geologic history of the Rashid-1 rover landing site, Atlas crater, inferred from a combination of orbital data analyses, telescopic spectropolarimetry and rheologic modelling.

Abstract

Located at 46.7°N, 44.5°E, Atlas is a well-known floor-fractured impact crater which records a complex volcanic history. Emplaced ~3.82 Gy ago within the lunar highlands, the 87 km diameter crater is characterized by the presence of collapsed walls, a rough and undulated floor marked with fractures, a ~ 1 km central peak complex, and two pyroclastic deposits. The evolution of Atlas crater is related to those of a nearby ~ 1.1 km high unnamed dome and of the Hercules impact crater, dated at 3.71 Gy. Cratering equations and rheological models were used to specify some aspects of the crater's geologic history. Atlas crater tapped into a pluton at a depth <13.5 km, dominated by mixed plagioclase, pyroxene and spinel VNIR signatures, and was later intruded by magma that stalled at ~ 2 km depth. Atlas crater lies in the center of a regional thermophysical anomaly measured in Diviner dataset, suggesting compositional or textural anomalies in the subsurface. The unnamed dome, emplaced by lavas as viscous as those forming known lunar silicic domes, could provide clues to this anomaly, as it may evidence the presence of more evolved alkalic or silicic rocks in the area. In addition, telescopic photometry and spectropolarimetry highlight the presence of more densely packed and either larger and/or rougher regolith grains in the pyroclastic deposits. Because of its high scientific value, Atlas was selected as the prime landing site of the Emirates Lunar Mission Rashid-1 rover, which made a hard landing on the Moon in April 2023.

Cite this article as: Flahaut, J., et al. (2026). Geology of Atlas crater, the prime landing site of the Emirates Lunar Mission Rashid-1 rover. *Planetary Research*, **1**(1), 274. https://doi.org/10.53480/4e7a-4y94

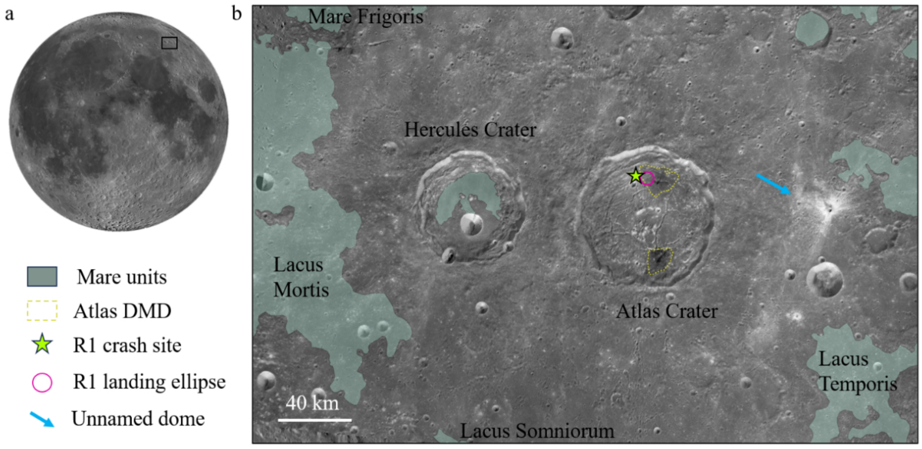

Figure 1 | (a) Location of Atlas and Hercules craters on the nearside of the Moon (LROC WAC global mosaic, orthographic projection centered at 0°N, 0°E). (b) Close-up on the Atlas region, bordered by Lacus Mortis to the west, Lacus Temporis to the east, and Lacus Somniorum to the south. The contours of the mare units from the LROC team are shown in green (mosaic of Kaguya TC orthoimages at 7.4 m/px, custom orthographic projection centered on the Emirates Lunar Mission Rashid-1 (R1) rover landing ellipse, i.e., at 47,52°N, 44,43°E (Flahaut et al., 2024)).

1 Introduction

Impact cratering and volcanism are two major geological processes shaping the surface of the Moon. Located southeast of Mare Frigoris, in the northeast lunar quadrant, the 87 km-wide Atlas crater (46.7°N, 44.5°E) evidences both processes. Atlas is a well-known floor-fractured impact crater (FFC), with a rough and undulated interior and concentric and radial fractures, which were interpreted as evidence for post-impact magmatic intrusions at depth (e.g., Schultz, 1976; Losiak et al., 2009; Jozwiak et al., 2012, 2015). Two dark patches are observed along floor fractures and were previously interpreted as dark mantling deposits (DMD) also referred to as pyroclastic deposits (e.g., Gaddis et al., 2003, 2012; Pathak et al., 2021). The crater topography is also marked by the presence of numerous blocks derived from a central uplift, as well as slumped, terraced walls (Figure 1). To the west of Atlas lies the 69 km-wide crater Hercules (46.8°N, 39.1°E), filled with mare deposits during the Eratosthenian (Grolier, 1974). About 100 km east of Atlas, an unnamed dome feature is observed (46.97°N, 49.50°E), possibly associated with anomalous rock compositions. The broader area, encompassing the unnamed dome and both Atlas and Hercules craters, was reported to display anomalously low nighttime temperatures and distinct thermophysical properties in Diviner data, consistent with so-called “cold spot regions” (Hayne et al., 2017; Cahill et al., 2019).

The geologic diversity of the Atlas-Hercules region made it an appealing landing site for the Emirates Lunar Mission (ELM) Rashid-1 rover. Launched in December 2022, Rashid-1 aimed to study the properties of lunar regolith, plasma interactions at the lunar surface, and, more generally, to advance our understanding of the Moon’s formation and evolution. To achieve this goal, the 10 kg ELM rover was equipped with two wide angle cameras provided by the French space agency CNES (CAM-1 and CAM-2), a microscopic imager (CAM-M), a thermal camera (CAM-T), four Langmuir probes (LNG), and a materials adhesion experiment (MAD) on its four wheels (Almarzooqi & S. AlMaeeni, 2021; Els et al., 2021). Four candidate landing sites were initially selected on the lunar nearside at 45°N latitude (± 7.5°) and were ranked based on their terrain characteristics and scientific value (Flahaut et al., 2024; Joulaud et al., 2024). Based on its geological diversity and strong scientific potential, an 8 km-diameter landing area located at ~ 47.52°N, 44.43°E within Atlas crater was selected as the prime landing site of the mission. Unfortunately, the commercial lander carrying the Rashid-1 rover failed to achieve a soft landing on the floor of Atlas on April 25th 2023, and the rover was therefore unable to complete its in situ investigation (Flahaut et al., 2024; Els et al., 2021).

The present paper describes the complex geological history of Atlas crater, as inferred from remote sensing data analyses, that led to its selection as the Rashid-1 rover prime landing site.

2 Dataset and method

A range of techniques, including remote sensing analyses of lunar orbiters data (Sections 2.1 to 2.3) and telescopic, spectropolarimetric observations (Section 2.5) were combined with rheologic modeling (Section 2.4) to infer the geologic and magmatic history of the area.

2.1 Available Dataset

Available remote sensing datasets from past and ongoing lunar missions were downloaded from the NASA Planetary Data System and JAXA's Selene Archive, processed and integrated into a Geographic Information System (GIS). The data collection includes: Kaguya Terrain Camera (TC) panchromatic images and associated Digital Terrain Model (DTM) (Haruyama et al., 2008), assembled as mosaics at 7.4 m/px, Lunar Reconnaissance Orbiter (LRO) Wide Angle Camera (WAC, 100 m/px) and Narrow Angle Camera (NAC, < 1 m/px) imagery and DTM (Robinson et al., 2010), Lunar Orbiter Laser Altimeter (LOLA) global Digital Elevation Model (DEM, resolution 118 m/px) (Smith et al., 2017), Lunar Prospector Gamma Ray Spectrometer (GRS) chemical maps at ~15 to 150 km/px (Lawrence et al., 1998), the Moon Mineralogy Mapper (M3) VNIR spectroscopic data (Pieters et al., 2009), Diviner rock abundance (Bandfield et al., 2011) and Christiansen Feature (CF) maps at ~240 m/px (Lucey et al., 2021), Miniature Radio Frequency (mini-RF) instrument circular polarization ratio (CPR) maps at ~240 m/px (Cahill et al., 2014) and the Clementine UV-VIS color ratio mineral (e.g., Heather & Dunkin, 2002) as well as Clementine-derived FeO and TiO_2 maps (e.g., Lucey et al., 2000).

2.2 Geologic mapping and dating

Using the available imagery and the previous geologic maps from Fortezzo et al. (2020) and Pathak et al. (2021), contours of the different geomorphologic units were drawn. Kaguya TC data were further used to derive surface ages by mapping impact craters on the rims and ejectas of both Hercules and Altas craters. Planetary surface dating is commonly performed through crater size frequency distribution (CSFD) measurements. This technique relies on the assumption that older surfaces have been exposed to impacts for longer and therefore accumulate more craters (e.g., Michael & Neukum, 2010; Michael et al., 2016). Crater sizes as well as the mapped crater-counted surface areas were compared to cratering models (Neukum et al., 2001), using Poisson statistics (as in Michael et al., 2016) and kernel estimators over binning or best-fit approaches (as in Robbins et al., 2018) to estimate the minimum model ages of both impact craters, using the routine of Breton et al. (2022). The resulting ages are then expressed as likelihood functions with associated intrinsic uncertainties (Breton et al., 2022).

2.3 VNIR spectroscopic analyses with M3

M3 VNIR spectroscopic data were processed following the method of Martinot et al. (2018) to derive mineralogical information across the study area. M3 spectroscopic data ranges from 430 to 3000 nm with 85 spectral channels and are available with a spatial resolution of ~ 140 to 280 m / pixel (Pieters et al., 2009). This study uses geometrically, photometrically, radiometrically and thermally corrected M3-Level 2 data (Boardman et al., 2011; Clark et al.,2011; Green et al., 2011; Besse et al., 2013) from the OP1B, OP2C1 and OP2C3 optical periods, which provide full coverage of Atlas crater. Mineral signatures are searched for in the 500-2700 nm range using spectral parameters (e.g., Mustard et al., 2011; Martinot et al., 2018). Selected pixel spectra are then compared with reference spectra from existing reference libraries (Kokaly et al., 2017; Pieters et al., 2004).

2.4 Rheologic modeling

Floor-fractured craters are evidence of a magmatic intrusion at depth. The resulting, uplifted crater topography can be used to infer the dimensions and depth of the intrusion, as well as to quantify its effects on the overlying crust. In the model of Jozwiak et al. (2012), a magma rises within the anorthositic crust until halted by a density boundary when reaching the brecciated lens that typically occurs beneath an impact crater. As magma reaches the brecciated lens low density zone, the intrusion stalls and propagates laterally, forming a laccolith (Figure 2). Using the crater topography (*wm*, *a*) and material constants (k, ɣm, Bm), Jozwiak et al. (2012) established an equation to calculate a theoretical driving pressure (Pd, in Pa) for the magma, in order to provide a quantitative assessment of the magmatic intrusion model:

$$Pd = wm \times ((2k/a) + m) \tag{1}$$

with:

wm = intrusion thickness, assimilated to the difference between the crater's theoretical unmodified depth (*dt*), and the current depth of the crater (*dc*), in meters,

a = axisymmetric radius of the intrusion, in meters,

k = magma yield strength (= 10^4 N/m^2, material constant derived by Johnson and Pollard, 1973),

ɣm = unit magma weight (= 4700 kg/m^2/s^2, material constant derived by Johnson and Pollard, 1973, assuming a magma density ρm = 2900 kg/m^3 and a lunar gravitational acceleration g = 1.62 m/s^2),

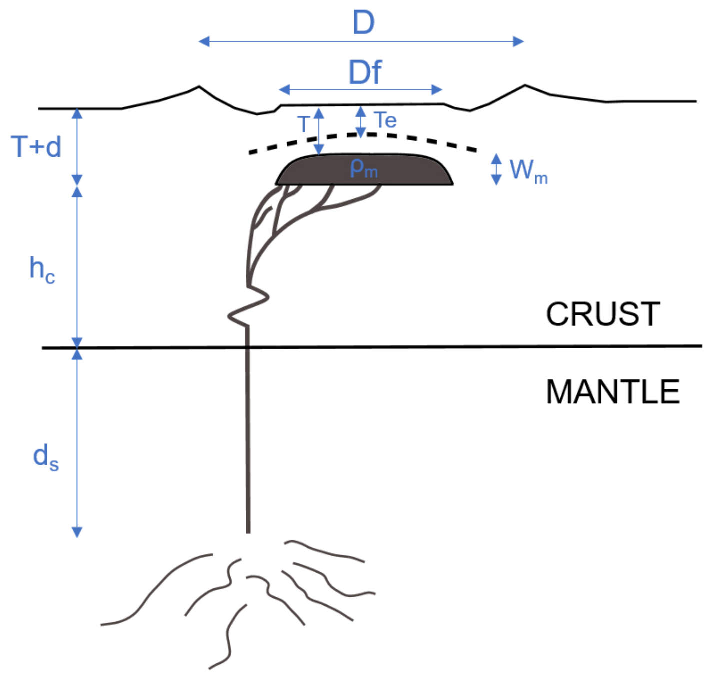

Figure 2 | Schematic representation of crater modification as a result of laccolith formation. Df is the crater floor diameter, used to represent the intrusion extent, and marked by either an uplifted region or the cohesive smooth crater floor unit. Wm is the thickness of the intrusion, taken to be the difference of the observed floor-fractured crater depth from the theoretical depth of an unmodified crater of the same size (Pike, 1980). hc is the length of the crustal magma column and ds is the length of the column past the Moho, although neither parameter was used in the calculation of magma overpressure (adapted from Wichman & Schultz, 1995).

Bm = elastic modulus of the country rock (= 7.47×10^{10} Pa, material constant derived by Johnson and Pollard, 1973).

The crater theoretical depth, *dt* (in km), can be calculated using Pike (1980)'s equation:

$$dt = 1.044 \times D^{0.301} \tag{2}$$

with: D = crater final diameter (in km).

From the driving pressure, Johnson and Pollard (1973) derived Equation (3) to further estimate the flexural thickness (*Te*, in km) of the overlying crust (or roof):

$$Pd = \frac{(5.33 \times wm \times \mathrm{Bm} \times Te^3)}{a^4} \tag{3}$$

We also performed modeling on the dome-like structure to assess the physical properties of the feeding lava flows, using equations from Wilson and Head (2003), Wöhler et al., (2007) and Schnuriger et al., (2020). Dome eruption can be considered as the extrusion of a Bingham fluid (the cooling magma), characterized by a yield strength τ (Equation (4)) and a plastic viscosity η (Equation (5)).

The yield strength τ (expressed in Pa) is given by:

$$\tau = (0.323 \times h^2 \times \rho\mathrm{d} \times \mathrm{g})/(Dd/2) \tag{4}$$

with:

ρd = magma density (variable in the literature, from 2000 kg/m^3 for foamy, rhyolitic magmas (Wilson & Head, 2003) to 2900 for kg/m^3 basaltic magmas (Wöhler et al., 2007),

Dd = average diameter of the dome in meters,

h = average height of the dome in meters.

The plastic viscosity η (expressed in Pa.s) is then given by:

$$\eta = 6 \times 10^{-4} \times \tau^{2.4}. \tag{5}$$

2.5 Telescopic photometry and spectropolarimetry

We used telescopic photometry (i.e., variations in brightness as a function of the geometry of acquisition) and spectropolarimetric imaging (i.e., measurements of the polarization state of the light as a function of wavelength) to visualize variations in the structural regolith properties across the region under study. Image data of the Atlas region at four different phase angles between 38° and 85° were acquired between February and April 2023 using a telescope of 200 mm aperture located near Dortmund, Germany, using an industrial-grade grayscale polarization camera combined with standard astronomical BVRI Johnson-Cousins broadband filters centered around visible and near-infrared wavelengths of 430, 520, 632, and 890 nm (Wöhler et al., 2024). Additional observations were conducted at four different phase angles between 4° and 30° in February 2024 with a telescope of 430 mm aperture at Mount Abu Observatory in Rajasthan, India, equipped with the same polarization camera and photometric filters.

To analyze the strength of the opposition effect (Hapke, 2012), we computed a phase ratio image (e.g., Shkuratov et al., 2010) of Atlas crater from our data acquired at small phase angles. The strength of the opposition effect is known to increase with increasing porosity of the regolith (Hapke, 2002). We thus computed the ratio between the I-band reflectances at phase angles of 4° and 9°.

The overall broad phase angle interval covered by our observations allows for a simultaneous estimation of polarimetric parameters at small and large phase angles. The typical dependence of the degree of linear polarization (DoLP) P on the phase angle α is depicted in Figure 3. It is commonly described by the empirical function $P(\alpha) = A\,(\sin\alpha)^B \left(\cos\left(\frac{\alpha}{2}\right)\right)^C \sin(\alpha\text{-}\alpha_{inv})$ (Equation 6, Goidet-Devel et al., 1995). The parameters A, B, C, and α_{inv} can be fitted easily to a set of observations using standard nonlinear optimization techniques.

The parameter α_{inv} denotes the phase angle at which the DoLP phase curve has a zero crossing. As apparent from Figure 3, five further intuitive polarization parameters can be inferred from a fitted DoLP phase curve:

- maximum DoLP $P_{max}>0$ typically occurring at phase angles around 90°,
- phase angle α_{max} at which P_{max} occurs,
- minimum DoLP $P_{min}<0$ occurring at phase angles between 0° and α_{inv},
- phase angle α_{min} at which P_{min} occurs,
- slope h of $P(\alpha)$ at $\alpha=\alpha_{inv}$.

These parameters have been suggested to characterize lunar surface terrains at both small (Shkuratov et al., 1992) and large phase angles (Shkuratov & Opanasenko, 1992). The polarization parameters P_{min}, α_{min}, α_{inv} and h, which depend on the DoLP behavior at small phase angles, have also been measured for a large set of asteroids (e.g., Bendjoya et al., 2022). Determining the parameters P_{max} and α_{max} requires observations at large phase angles, which are not available for many asteroids due to geometric constraints. They have been obtained for several comets, though (e.g., Kiselev et al., 2015), but despite the observed similar DoLP phase curves, observations of cometary dust are not directly comparable to observations of lunar and asteroid regolith as the latter material has a much higher packing density.

An important relation needed for the polarimetric analysis is the Umov law (e.g., Shkuratov and Opanasenko, 1992), stating that the maximum DoLP P_{max} decreases with increasing albedo of the surface material. The commonly accepted explanation for this effect is that the light reflected by the regolith becomes increasingly dominated by light scattered multiply between several regolith grains when the albedo increases, where each scattering process leads to a partial depolarization. As a proxy for the surface albedo, we used the spectral reflectance measured by the M3 instrument at 890 nm wavelength (M3 channel 16). The reflectance data were resampled to a resolution of 1.5 km/pixel, corrected for topography, and normalized to 30° incidence angle and 0° emission angle (Wöhler et al., 2014, 2017; Wohlfarth et al., 2023). The relation between P_{max} and reflectance can be described by a power law (Shkuratov & Opanasenko, 1992; Wöhler et al., 2024).

The Umov law does not describe the P_{max} vs. reflectance relation perfectly, as positive and negative deviations of P_{max} are clearly apparent. Their classical interpretation according to Shkuratov and Opanasenko (1992) is in the way that a positive deviation ("excess") of P_{max} indicates a larger-than-average and a negative deviation a smaller-than-average regolith grain size, respectively. An empirical calibration of the P_{max} deviation with respect to grain size was provided by Shkuratov and Opanasenko (1992).

Laboratory studies of returned lunar samples have shown that typical regolith grain sizes correspond to several tens of micrometers (e.g., Dollfus, 1998), which is about two orders of magnitude larger than the wavelengths of visible light. Theoretical studies have shown that smooth particles in that size range

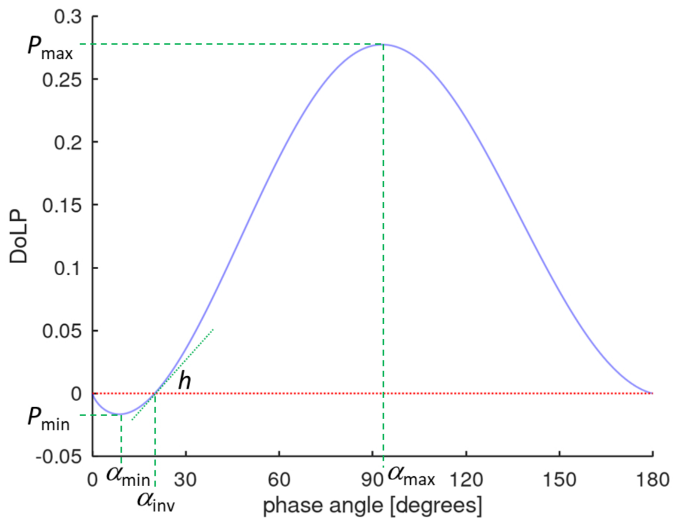

Figure 3 | Typical DoLP phase curve according to the empirical function introduced by Goidet-Devel et al. (1995). The inferred polarization parameters are indicated.

hardly have an effect on the polarization of scattered light in the visible domain, but that the main contribution to the observed polarization is generated by structures of about 0.1–1 µm size (Zubko et al., 2020). As the lunar regolith is not dominated by such small grains, a physically plausible source of the observed deviations from the Umov law may be the roughness of the regolith grain surfaces on sub-micrometer scales.

Our telescopic observations allow for a pixel-wise determination of a set of six polarization parameters in four spectral bands, i.e., 24 parameters altogether. We applied a principal component analysis (PCA) (e.g., Marsland, 2015) to our data set and constructed an RGB composite of the scores on the first two principal components, which visualizes differences in the spectropolarimetric properties of the regolith in a compact way. Clustering this three-dimensional dataset with the self-organizing map (SOM) method (e.g., Marsland, 2015) yields an unsupervised subdivision of the study area into nine classes that clearly correspond to different terrain types, such as mare, highland, pyroclastic deposits and fresh crater materials. The clustering procedure also yields a set of prototypes representing the average spectropolarimetric parameters of these classes.

3 Results

3.1 Geologic mapping and dating

Atlas crater lies within the Geminus quadrangle of the Moon, where mature highlands have been mantled by nearly continuous blankets of ejecta from the Serenitatis, Crisium, Humboldtianum, and Imbrium basins, which lie southwest, southeast, and west of the quadrangle, respectively. Early stratigraphic mapping placed the formation of large craters (Franklin, Atlas, Cepheus, Geminus and Hercules, in that order) and the emplacement of mare unit between the early Imbrian to Eratosthenian time (Grolier, 1974).

Atlas is a prominent complex impact crater with a final rim-to-rim diameter of 87 km and an average depth of 3.4 km. The floor of Atlas crater is characterized by the presence of both concentric and radial fractures, a ~ 1 km high semicircular-shaped central peak complex, and two pyroclastic deposits covering ~ 420 km^2 (North) and 260 km^2 (South) (surface areas estimated from the M3 spectral parameters map) (Figure4a). Possible feeding vents are recognized in wider segments of floor fractures, with a local concentration of the lowest reflectance material. Dislodging of material from the crater walls by gravity has produced slumped walls and extended terraces all along the crater rim. The terrace zones form linear features parallel to the crater walls which give a staircase-like appearance and likely correspond to normal faults. Most of the central part of the crater is made of hummocky terrains, collapsed pits, and fractures. At a smaller scale, the crater floor is smoother with gentling rolling plains, relatively devoid of impact craters, as observed within the Rashid-1 landing ellipse (Flahaut et al., 2024; Joulaud et al., 2024). M3 data suggest that the eastern part of the crater is partially blanketed by the ejecta of the nearby Hercules crater. CSFD measurements yield an age of 3.82 ± 0.03 Gyr (Early Imbrian) and 3.71 ± 0.03 Gyr (Late Imbrian) for Atlas and Hercules craters, respectively (Fig. 4b,c and Fig. 5b).

About 100 km east of Atlas crater, the presence of a ~1100 m high, 15 km wide viscous dome (centered at 46.97°N, 49.50°E) is evidenced by optical, spectral, and topographic data. The dome appears of higher

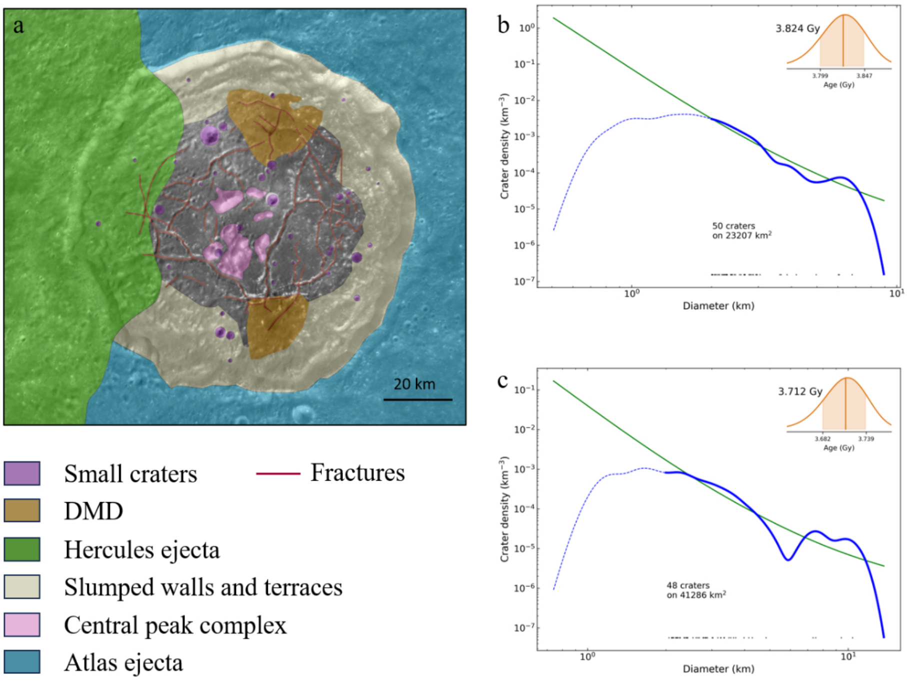

Figure 4 | (a) Geomorphological sketch map of Atlas crater, overlain (semi-transparently) on Kaguya TC orthoimages. (b) Crater size-frequency distribution for Atlas crater (blue curve). The green curve represents the best-fit isochron using the model of Neukum et al. (2001), and the orange curve gives the most likely model age and its associated uncertainty. (c) Dating Hercules crater using the same approach.

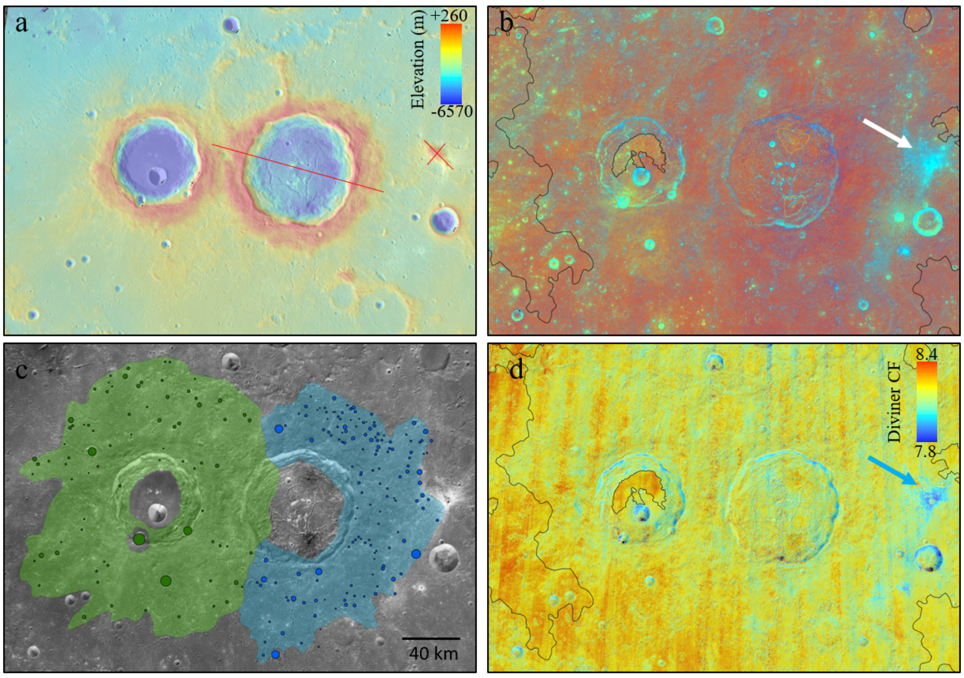

Figure 5 | (a) Topographic map of the study area from Kaguya TC. The red lines indicate the location of the topographic profiles shown in Figure 7. (b) Clementine color ratio mineral map displaying yellow/orange hues in mare areas (black outlines), red/purple hues in mature highland areas, and cyan around fresh impact craters and the unnamed dome (arrow). (c) Crater counts used for the dating of Atlas and Hercules craters. (d) Diviner CF map displaying lower values for the unnamed dome (arrow) and fresh impact craters and higher values in mare areas (Lucey et al., 2021).

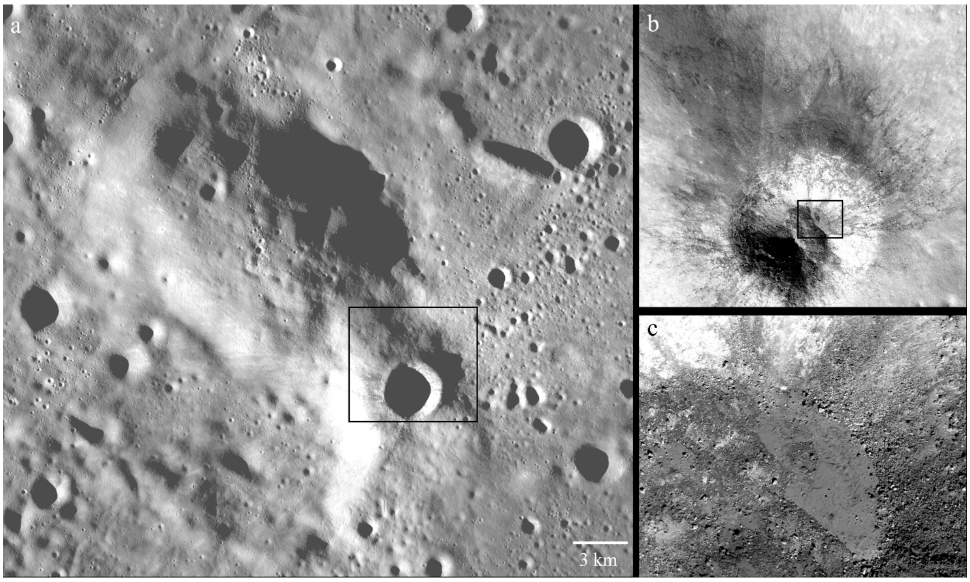

Figure 6 | (a) Kaguya TC evening image of the unnamed dome. The black box indicates the location of panel (b). (b) Close-up view of the 3 km diameter crater at the southern end of the dome (NAC image M1414880576). Dark splashes of melt are visible on the crater wall and extend well beyond its rim, onto the dome surface, where they form dark superposed lobes. The black box indicates the location of panel (c). (c) Close-up view of a ~200 m wide impact melt pond at the bottom of the simple crater (NAC image M141932532).

albedo on the WAC and Kaguya panchromatic images, as do two fresh impact craters located at (44.36°N, 48.71°E) and (44.43°N, 47.63°E) southeast of Atlas crater (Figure 5). The dome itself is overprinted by a relatively fresh, 3 km-diameter Copernican crater and is largely covered by its ejecta and secondary craters, making it difficult to assess whether the dome is intrusive or extrusive. NAC imagery of the fresh crater reveals the presence of relatively light-toned rocks in the crater walls, covered by darker splashes and boulders, likely originating from the impact crater's melt itself (Figure 6). Both darker, boulder-rich patches and lighter-toned rocks crop out along the walls of the 22 km-diameter Atlas A. crater (45.32°N, 49.57°E), suggesting a complex subsurface layering.

3.2 Rheologic modeling

Using Equation (2) and a final crater diameter of D = 87 km, the theoretical depth of Atlas is dt = 4.0 km, while topographic data suggests a present depth dc = 3.42 km (Figure 7a); the thickness of the intrusion in Atlas is therefore wm = 600 m. With a measured intrusion radius of a = 29 km (Figure 7a), the magmatic driving pressure Pd and the effective flexural thickness Te are estimated at 2.8×10^6 Pa and 2.0 km, respectively.

Using Equations (4) and (5) with an average dome height of 1100 m and an average dome diameter of 15 km (Figure 7b), the yield strength and viscosity of the feeding flow are estimated at $\tau = 1.7 \times 10^5$ Pa and $\eta = 2.1 \times 10^9$ Pa.s for a magma density ρd = 2000 kg/m^3 (value previously used in models of Wilson & Head, 2003) assuming a foamy, silica-rich magma) and $\tau = 2.4 \times 10^5$ Pa and $\eta = 5.1 \times 10^9$ Pa.s for a typical basaltic magma density ρd = 2900 kg/m^3.

3.3 Spectroscopic analyses

Clementine color ratio mineral maps (red/purple hues, except for cyan around fresh impacts) and Diviner CF values (8.15 µm on average) suggest the presence of dirty and/or mature highland material on the floor of Atlas crater (Fig. 5b,d). M3 spectra of the crater floor and walls are usually relatively featureless (e.g., showing no absorption features across the 600 to 2700 nm range investigated). Locally, spectra with two absorption bands centered at ~930 nm and 1940 nm, diagnostic of low-calcium pyroxenes (LCP), are observed. Plagioclase signatures, evidenced by a broad 1310 nm spectral feature, are also present around fresh craters in both the northern and eastern parts of the crater floor.

Both pyroclastic deposits show similar spectra, with broad features centered at 970 and 1900 nm, consistent with LCP and/or green glass (Fig. 8e,g). Diviner CF values of 8.2 within the DMD suggest the presence of mafic components.

The central peak of Atlas crater shows diverse mineral signatures with spectra of LCP (bands at 910 + 1980 nm), pigeonite (bands at 950 + 2057 nm), high calcium pyroxene (HCP) and/or spinel (band at 970 nm + deeper band at 2140 nm), and mixed plagioclase + pyroxene (with composite features located around 950, 1310, 2000 nm) (Fig. 8e).

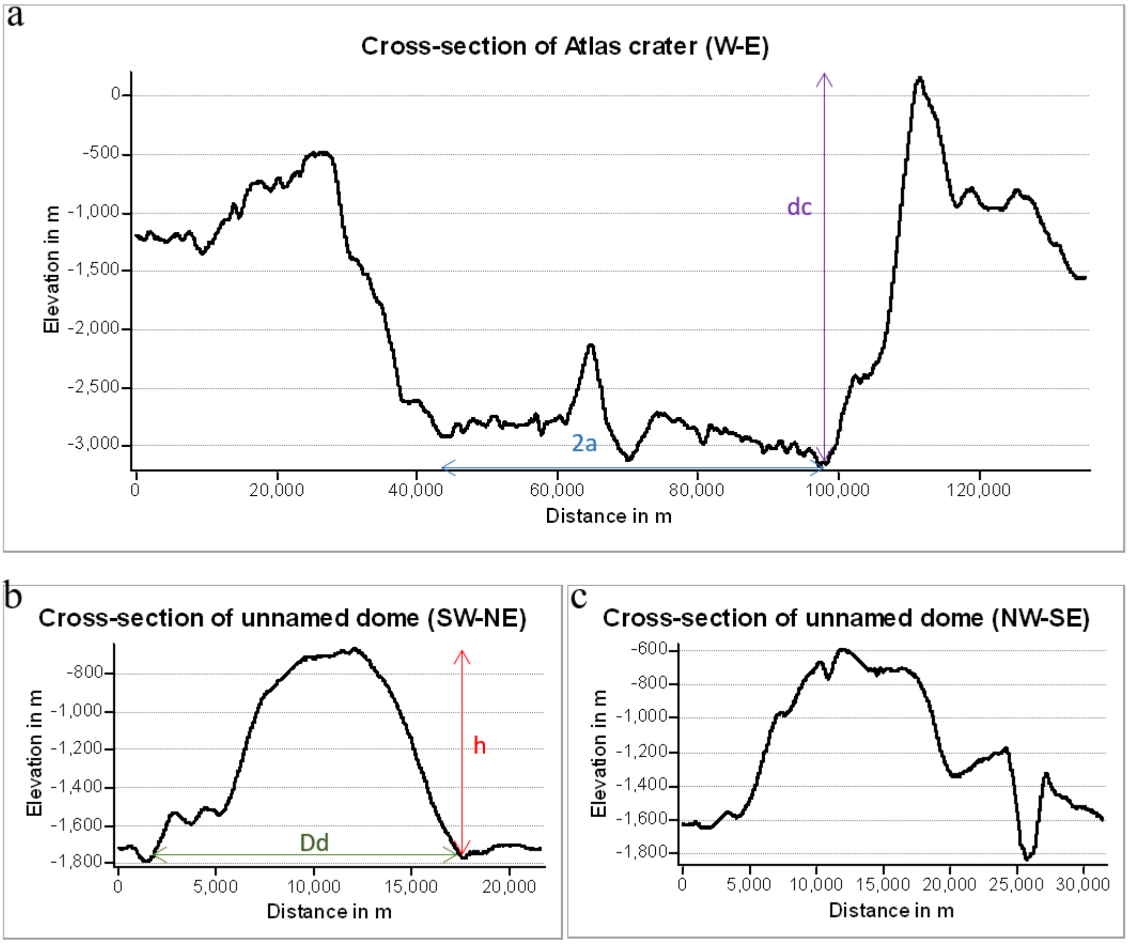

Figure 7 | (a) Topographic profiles of Atlas crater and the unnamed dome from Kaguya TC DTM (see Fig. 4 for cross-section locations). Measured morphometric parameters are: *dc* = current depth of the crater (3.42 km); *a* = axisymmetric radius of the intrusion, in meters (29 000 m); *Dd* = average diameter of the dome in meters (15 000 m); *h* = average height of the dome in meters (1100 m).

Clementine color ratio mineral maps show light blue tones, and Diviner data indicate low CF values (down to 7.7 µm) in the southern half of the dome and around the two fresh impact craters southeast of Atlas (Fig. 5b,d). M3 spectra over the dome summit display two broad absorption bands centered around 930 and 1938 nm, consistent with LCP, as do the dome surrounding terrains. Distinct spectra with broad features centered at 910 and 2217 nm are observed over the darker melt deposit of the 3 km diameter Copernican crater, whereas the brighter wall rocks display a weak, broad feature centered at 2097 nm, possible indicative of spinel. The impact crater located at 44.36°N, 48.71°E, south of the dome, is characterized by the presence of absorption bands centered at 950 and 2057 nm in its fresh ejecta blanket, consistent with an intermediate pyroxene composition such as pigeonite (Fig. 8f).

3.4 Photometric and spectropolarimetric analyses

The constructed I-band phase ratio image obtained from the intensity data at phase angles of 4° and 9° is shown in Figure S2. Both pyroclastic deposits within Atlas crater stand out as negative phase ratio anomalies, whereas the small fresh crater to the west of the northern deposit appears as a small positive anomaly. Maps of the M3 spectral reflectance at 890 nm and the maximum DoLP P_{max} in the I band are shown in Figure 9 panels (a) and (b), respectively. The power law fitted to the $\log_{10}(R)$ vs. $\log_{10}(P_{max})$ data points is shown in Figure 9c. In the map of the deviation of P_{max} from the fitted Umov law (Fig. 9d), most of the flat floor of Atlas crater does not appear to differ from the surrounding highland terrain. The southern pyroclastic deposit stands out as a strong positive anomaly, whereas the northern pyroclastic deposit is less conspicuous. The dark mare fill in the northern part of the floor of Hercules crater corresponds to a moderate positive anomaly.

Our clustering analysis reveals the typical wavelength-dependent behavior of the inferred polarization parameters (Figure 11). To our knowledge, this is the first lunar regional high-resolution multispectral polarization study of this kind. For all derived clusters, the parameter P_{max} is highest in the B band, lowest in the V band, and increases slightly again in the R and I bands. The phase angle α_{max} of maximum polarization lies between 80° and 100° in the B, V and R bands but decreases to 75°–80° in the I band. The

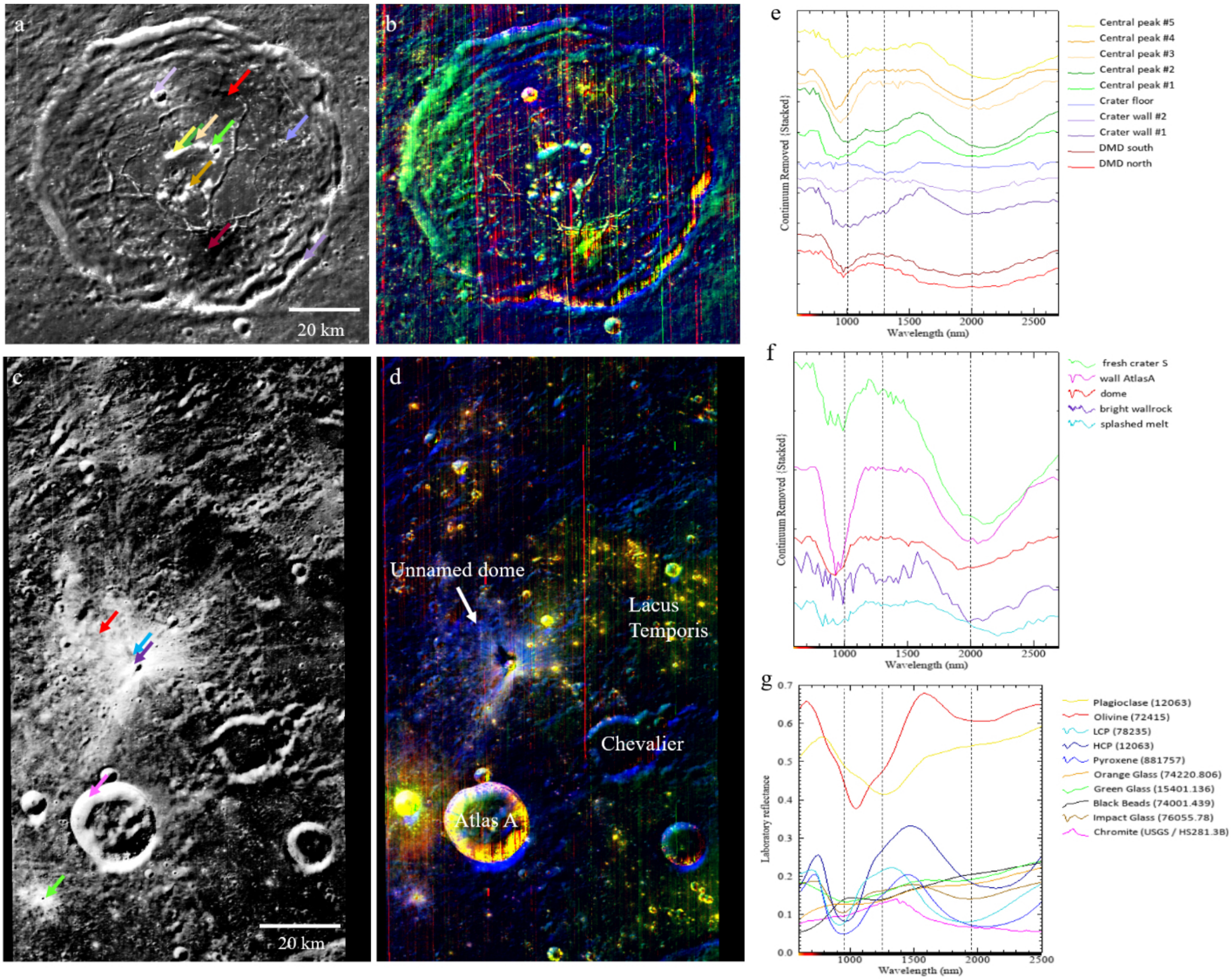

Figure 8 | (a) M3 reflectance at 750 nm in Atlas crater (mosaic of images M3G20090729T193219 and M3G20090729T233354; stretched values: 0.046-0.129). The colored arrows indicate the locations of the spectra shown in Figure 7e. (b) RGB composite of M3 summary parameters IBD1000 (stretched values: 27.04–27.43), IBD2000 (stretched values: 22.2–22.706), and R1580 (stretched values: 0.070–0.273), highlighting the presence of pyroxene and plagioclase in yellow and magenta tones, respectively. (c) M3 image M320090729T1044248 (covering the unnamed dome), reflectance at 750 nm (stretched values: 0.062–0.184). The colored arrows indicate the locations of the spectra shown in Figure 7f. (d) RGB composite of M3 summary parameters IBD1000 (stretched values: 27.06–29.42), IBD2000 (stretched values: 22.1–27.36), and R1580 (stretched values: 0.010–0.509). (e) M3 spectra (continuum removed) collected over regions of interest (DMD, crater wall) and from regions of 5 × 5 pixels. Corresponding raw spectra (prior to continuum removal with ENVI) are shown in Figure S1. Vertical bars at 1000, 1300, and 2000 nm are included to guide identification of the main absorption bands of pyroxenes and plagioclase feldspars. (f) M3 spectra (continuum removed) collected over regions of 5 × 5 pixels on the unnamed dome and its surroundings. (g) Reference spectra from existing spectral libraries are shown for comparison. All reference spectra were downloaded from the RELAB spectral library and were acquired on lunar (Apollo) samples, except for the terrestrial chromite spectrum that originates from the USGS library.

negative polarization is weakest in the V and R bands ($|P_{min}|$ between 0.012 and 0.016) and strongest in the I band ($|P_{min}|$ >0.02). The behavior of h follows that of $|P_{min}|$, and the phase angle α_{min} of minimum polarization decreases from ~13° in the B band to ~9° in the I band. Similarly, the phase angle of inversion α_{inv} decreases from ~28° in the B band to ~23° in the I band.

The RGB color composite in Figure 10a depicts the scores on the first three principal components derived from the pixel-wise spectropolarimetric parameters. The cluster index map (Figure 10b) shows a clear distinction of the pyroclastic deposits from the surrounding crater floor material. Both deposits belong to cluster 6 (yellow), and the center of the southern deposit to cluster 3 (medium blue), corresponding to the highest levels of P_{max} and $|P_{min}|$ (Figure 11). Mare areas to the west and southwest of Atlas crater are also assigned to cluster 6. The ejecta blanket of the small crater to the west of the northern deposit is assigned to clusters 1 (dark blue) and 4 (cyan); the latter stands out by its particularly weak negative polarization $|P_{min}|$. Highland-like areas in the northern part of the crater floor and to the east

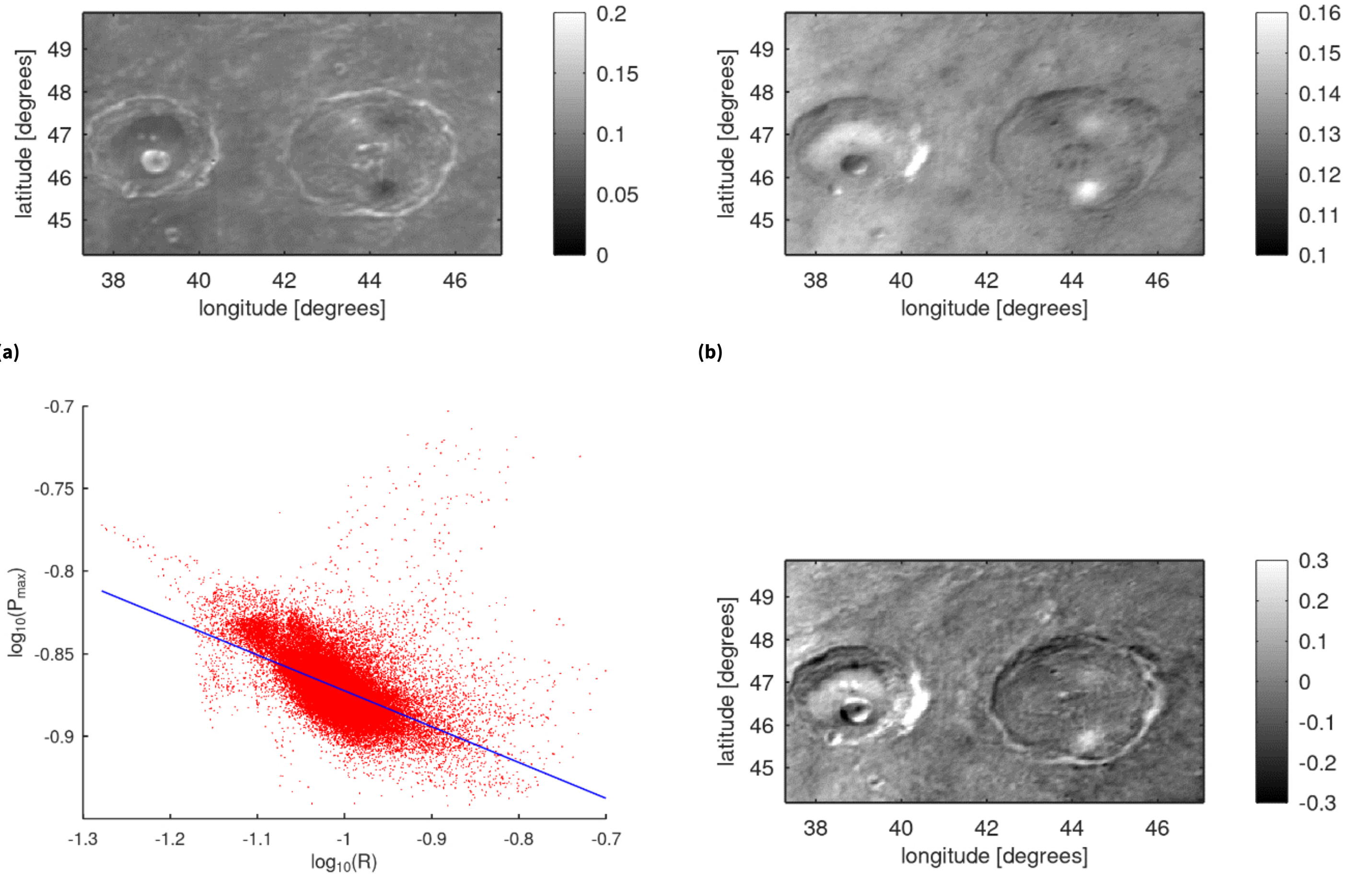

(a) (b) (c) (d)

Figure 9 | (a) M3 spectral reflectance (890 nm, channel 16) corrected for topography and normalized to 30° incidence angle and 0° emission angle (Wohlfarth et al., 2023). (b) Maximum DoLP P_{max}. (c) Double-logarithmic diagram of P_{max} vs. reflectance with best-fit power law. (d) Deviation of P_{max} from power law, converted to decadal logarithmic relative grain size (Wöhler et al., 2024), using the calibration by Shkuratov and Opanasenko (1992).

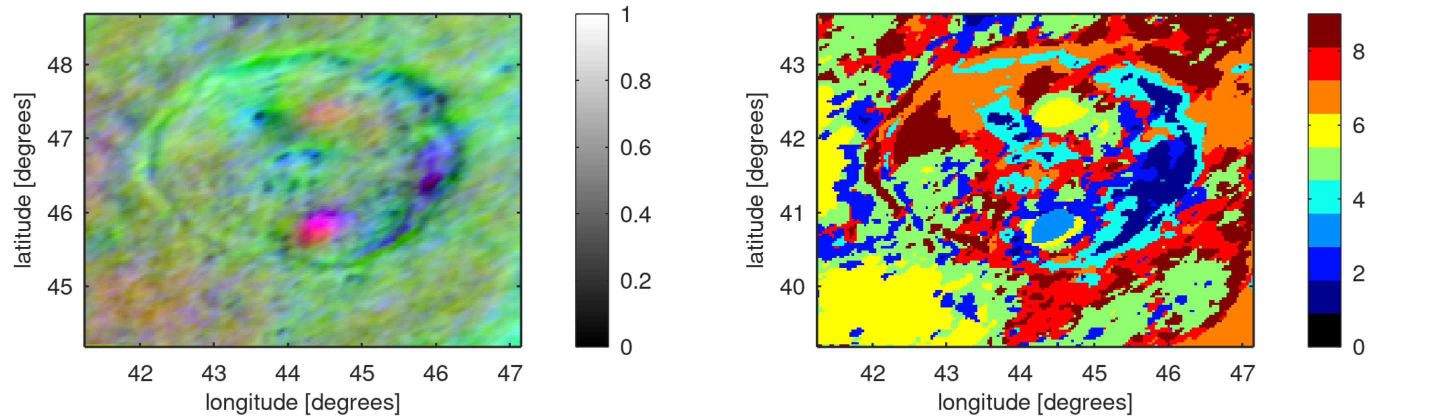

(a) (b)

Figure 10 | (a) RGB composite of the scores on the first two principal components inferred from the distribution of the 24 spectropolarimetric parameters. (b) Cluster index map obtained by self-organizing map clustering of the scores on the first two principal components.

of the crater belong to clusters 1, 4, and 7 (orange). Clusters 5 (light green), 8 (red), and 9 (brown) denote materials with intermediate polarimetric properties, corresponding to mixed mare and highland materials.

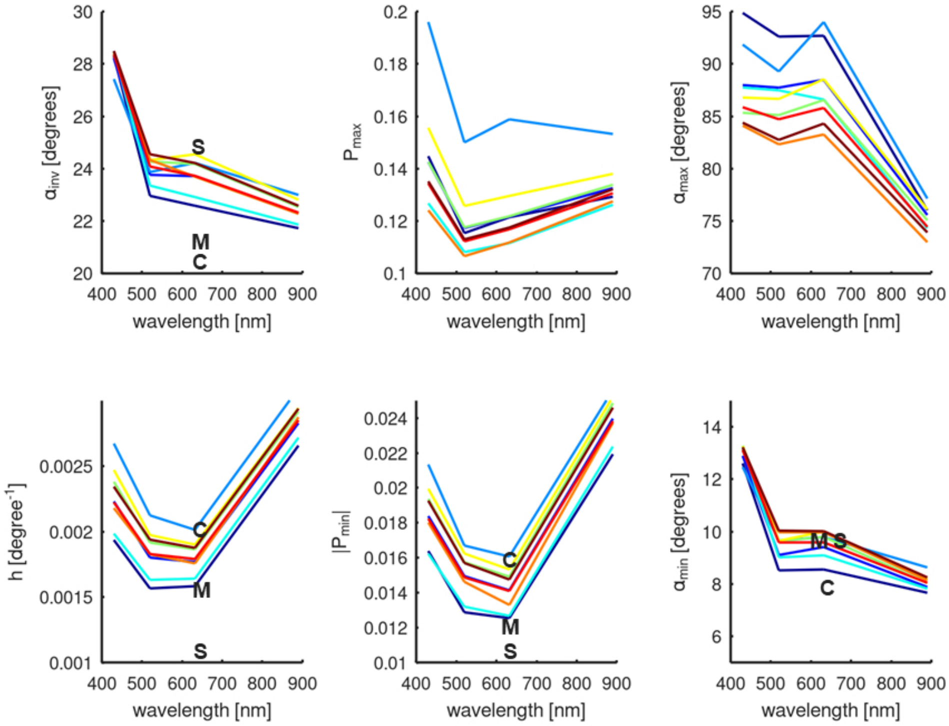

Figure 11 | Cluster prototypes of the PCA+SOM analysis of the spectropolarimetric parameters. The curve colors correspond to those in the cluster index map of Figure 10. The letters denote typical R-band polarimetric parameter values observed for asteroids of classes S (iron/nickel mixed with silicates), M (iron/nickel) and C (carbonaceous chondrites). Data from Bendjoya et al. (2022), asteroid classes from Prasad and Das (2024).

4 Discussion

4.1 Intrusive magmatic activity at Atlas crater

The region of Atlas crater records a complex volcanic history, as indicated by the composition of the crater's central peak, the uplifted and fractured floor (both suggestive of intrusive volcanism), and surface expressions of mare volcanism in nearby Hercules crater and the surrounding plains, thought to be associated with both fire-fountains and viscous, dome-forming, eruptions.

Rheologic modeling of the floor-fractured crater suggests the presence of a shallow magmatic intrusion at a depth of ~ 2 km, with a thickness of ~ 600 m, that we approximate as a lens-shaped body with a radius of ~ 29 km. Results from our rheologic modeling are within the range reported for other floor-fractured craters: for example, Taruntius (D = 59 km, wm = 880 m, Te = 0.92 km) and Gassendi (D = 110 km, wm = 1970 m, Te = 4.2 km) (Jozwiak et al., 2012).

Diverse mineralogical compositions (mixed pyroxene and plagioclase, and possible spinel inferred from VNIR spectroscopy) in the central peak complex of Atlas also suggest the presence of an underlying pluton. While previous analyses by Pathak et al. (2021) reported the presence of olivine in shadowed areas of the central peak, olivine is not detected with certainty here. These authors also argued for the presence of hydration features associated to the central peak mafic minerals. However, their thermal correction of the M3 dataset does not follow the PDS standard (Clark et al., 2011) and remains debated (e.g., Wöhler et al., 2017; Wohlfarth et al., 2023). As there is currently no consensus on the removal of thermal effects at longer wavelengths, the M3 channels > 2700 nm are purposely not analyzed in our study.

Using equations from Cintala and Grieve (1998), the minimum depth of origin of the material in the central peak can be approximated as equal to the depth of melting (e.g., Flahaut et al., 2012), which in Atlas crater would be ~ 13.5 km. Hence, there is evidence for at least two volcanic intrusions beneath Atlas crater: (1) a pluton with spinel-bearing lithologies at depths < 13.5 km, already present at the time of the impact, 3.82 Gy ago, (2) a shallow intrusion at a depth of ~ 2 km which post-dates the crater's emplacement and uplifted its floor.

Another important implication of FFC formation by magmatic intrusion is the subsequent cooling, evolution, and degassing of the laccolithic magma which can be associated with venting and pyroclastic eruptions (e.g., Head & Wilson, 1979; Jozwiak et al., 2015; Wilson and Head, 2017). Volatile accumulations exceeded the tensile strength of the overlying crater floor would result in localized explosive, vulcanian eruptions emplacing both fine-grained juvenile and non-juvenile material. Previous studies predict that associated pyroclastic deposits will be localized along fractures, specifically near the periphery of the crater floor, where subsidiary diking from the intrusion is most likely to occur (Jozwiak et al., 2015).

Despite previous evidence for multiple laccoliths beneath Atlas crater, GRAIL Bouguer anomalies and gravity maps only display regional variations, mainly related to the presence of the mare units of Lacus Mortis to the west and Lacus Temporis to the east. Crustal thickness models return values of ~ 30 km, close to the average thickness of the lunar crust (e.g., Wieczorek et al., 2013).

4.2 DMD formation by vulcanian eruptions

Spectral analyses of lunar DMD at a global scale have uncovered a wide compositional diversity among deposits (e.g., Gaddis et al., 2000, 2003; Besse et al., 2014; Misra et al., 2026) which evidence varying modes of emplacements (e.g., Head and Wilson, 2017). Whereas regional DMD have been argued to form as the result of either strombolian or hawaiian eruptions, localized DMD such as the ones in Alphonsus crater have been interpreted as evidence for vulcanian eruptions (Head and Wilson, 1979, 2017; Gaddis et al., 2003). In the latter, the explosion of a solid, near-surface plug of wall-rock material at the top of a dike would result in proximal accumulation of coarse clasts with limited dispersion of fine ash material (Head and Wilson, 2017; Keske et al., 2020).

DMD in Atlas crater were previously described as small-scale pyroclastic deposits, with a highland component mixed with fragmental basalt and a low glass content (Gaddis et al., 2003, 2012). Our spectral analysis of both deposits is consistent with VNIR signatures of LCP and/or green glass, although the north and south pyroclastics show different albedos and TiO_2 contents. Diviner CF values are slightly more elevated than those of the crater floor, and could be consistent with mixed bedrock and juvenile (i.e., inherited from the eruption magma, glass or crystalline basalt) material. Hence Atlas pyroclastic deposits could be, as in Alphonsus crater, products of a vulcanian eruption. Analyses of both photometric and spectropolarimetric data confirm that the pyroclastic deposits differ from mare basalts, with a distinct porosity, grain size or roughness, and/or glass content (see next section).

The phase ratio image (Fig. S2) shows that both pyroclastic deposits on the floor of Atlas crater exhibit a weaker opposition effect than the surrounding crater floor material, implying a less porous and more compact regolith. This behavior indicates a peculiar fine structure of the pyroclastic material that differs from the mare material to the west and southwest of the crater, which were presumably emplaced by lava effusion rather than explosive eruption. In contrast, the high phase ratio value of the small bright crater to the west of the northern deposit suggests a higher-than-average regolith porosity. This is likely due to recent formation of the crater, such that the regolith has not yet been significantly compacted by impact gardening.

According to the classical interpretation of the deviations of P_{max} from the fitted Umov law, the observed behavior shown in Figure 9d would indicate regolith grains that are larger than those in the surrounding terrain by a factor of ~2 in in the southern and by a factor of ~1.3 in the northern pyroclastic deposit. Alternatively, an interpretation in terms of grain-surface roughness would imply the regolith grains of the pyroclastic deposits have rough, angular surfaces, thus providing many scatterers on submicrometer scales and producing the observed polarization signature. Both interpretations are consistent with an exceptionally high mechanical strength of the pyroclastic material, especially in the southern deposit, preventing extensive grinding of large regolith grains or smoothening of the grain surfaces by micrometeoroid impact gardening. These unusual mechanical properties are likely the consequence of the high content of non-juvenile (i.e., inherited wall rock) material in the pyroclastic material, akin to its emplacement as a vulcanian eruption.

4.3 The Atlas region – a unique cold spot feature

Spectropolarimetric data do not show any difference between the floor of Atlas crater and the surrounding terrains, but they were not acquired at a scale large enough to allow comparison to other regions of the lunar surface. Previous remote sensing investigations have shown that Atlas crater is the center of a large-scale, unexplained, low thermal inertia pattern referred to as a “cold-spot”, indicating it could be an atypical lunar terrain. Most lunar cold spots correspond to very fresh (Copernican) impact craters, which have modified the surrounding regolith out to distances of ~ 10–100 crater radii, increasing rock abundance and thermal insulation and thus producing colder nighttime temperature (e.g., Bandfield et al., 2014; Hayne et al., 2017). A few cold spot anomalies are also reported in association to low rock abundance and fined-grained, glassy material of Aristarchus pyroclastic deposits (Hayne et al., 2017). However, the Atlas region does not belong to any of the pervasive pyroclastic deposits or young impact categories, which could explain the thermophysical anomaly. The thermophysical anomaly also extends over a much larger scale than other reported cold spots and suggests a low density or high porosity (fluffy) regolith over an area > 500 km × 300 km (Cahill et al., 2019).

Previous analyses of the regolith properties at the Rashid-1 landing site within Atlas crater by Joulaud et al. (2024) yielded a relatively low regolith thickness estimate (~1.2 m on average within the landing ellipse), well below the average values for lunar highlands, with a peculiar regolith texture: few craters are visible at the NAC scale, but boulders are frequent both on the crater floor, and within the fractures (Gaddis et al., 2012). High rock abundance is also observed in the walls of smaller craters south of Atlas and could indeed confirm the presence of a shallow bedrock or coarser regolith.

Additional clues to the origin of this peculiar cold spot signature may come from the complex volcanic history of Atlas crater. In addition to experiencing multiple intrusions, the region could be associated with anomalously evolved rock compositions, as described in the next section.

4.4 Potential evidence for evolved rock compositions

With an estimated viscosity on the order of 10^9 Pa.s, the lava feeding the unnamed dome east of Atlas crater is as viscous as the ones that erupted at both the Gruithuisen (Wilson & Head, 2003) and Mairan (Wöhler et al., 2007) domes, and 3-5 orders of magnitude more viscous than lavas that form typical mare domes (e.g., Schnuriger et al., 2020). Both the Gruithuisen and Mairan domes have been identified as high-silica features based on their relatively low CF values in the Diviner TIR data (e.g., Greenhagen et al., 2010; Glotch et al., 2010). The dome identified east of Atlas also displays CF values lower than its surroundings, although its surface is contaminated by the ejecta and secondary impacts derived from a 3 km diameter fresh impact crater occurring at its southern end (Figs. 5, 6c), which complicate the interpretation of the Diviner signal. Although the CF is sensitive to the average silica polymerization, and hence seems particularly well-suited for investigating feldspar compositions and quartz occurrences, it has unexpectedly been found to be affected by space weathering (an effect that was not anticipated before the LRO/Diviner mission, e.g., Greenhagen et al., 2010; Lucey et al., 2021). Hence, despite advanced corrections of the soil maturity effect using the OMAT index calculated from VNIR data, fresh impact craters may in some cases still display lower CF values that more mature, surrounding terrains (Lucey et al., 2021).

Low CF values of ~8.0 (below the typical highland value of 8.15) are observed around three fresh impact craters east and south of Atlas crater and correspond to cyan colors on the Clementine color ratio mineral map, lower FeO abundances and higher albedo material on the Clementine, M3 750 nm band and LROC WAC images (Figs. 4, 5). Coupled with the presence of a highly viscous extrusive dome, it is tempting to interpret these signatures as possible evidence for distinct mineralogical compositions, either with more alkaline feldspar / alkali-rich anorthosites or silicic rocks. However, the CF position is also known to be affected by the intensity of the subsurface thermal gradient (Lucey et al., 2021), which seems to differ from the rest of the lunar surface in the Atlas region. Hence, the CF value cannot uniquely confirm the presence of silica or evolved feldspathic composition.

Investigations of additional datasets probing other ranges of the electromagnetic spectrum could be used to test the presence of evolved composition, for instance in viscous domes, in the near future. Using far ultra-violet data from the LRO Lyman Alpha Mapping Project (LAMP) instrument, Czajka et al. (2023) reported the presence of Off/On-band ratios consistent with shocked and possibly alkalic plagioclase feldspars in the central peak and high albedo ejecta of the Aristarchus Crater. Microwave emission maps from the Chang'E-2 mission were also used for the first time to infer the presence of a granitic batholith in the Compton-Belkovich farside area, based on its elevated geothermal heat flux (Siegler et al., 2023). Elemental abundances maps (e.g., Th, Al, Fe) derived from GRS and Clementine maps provide limited additional constraints, due to the location of Atlas on the very edge of the Procellarum KREEP terrane (PKT). Indeed, the region is characterized by typical intermediate values between the PKT mare units and the farside highland units. Evidence for both higher albedo rocks, and dark, boulder-rich (pyroclastic?) material is present in the walls of small craters and the Atlas A crater south of the unnamed dome, but has yet to be further investigated with LROC NAC imagery acquired under variable illumination conditions.

Notably, granites are rare on the Moon, and suggest re-melting of basaltic intrusive bodies (e.g., Hagerty et al., 2006; Seddio et al., 2013), although alternative formation mechanisms have been proposed, such as liquid-silicate immiscibility (e.g., Rutherford et al., 1976) or in situ differentiation of mafic magmas (e.g., Neal and Taylor, 1989). Whether the central peak of Atlas crater could be sampling a granitic pluton is difficult to assess, as the spatial resolution of the Diviner instrument is limited to 240 m/px, and the CF calculation is known to be affected by slope (e.g., Greenhagen et al., 2010). However, the central peak of Atlas does not show anomalous CF values. Minerals identified from VNIR spectroscopy in the central peak may indicate the presence of spinel-bearing anorthosite, or more mafic rocks, as well as lunar felsites (which are, based on Apollo sample analyses, dominated by plagioclase feldspars + silica + LCP and/or HCP; e.g., Seddio et al., 2013). In any case, Atlas crater records multiple stages of intrusion, which could have led to (partial) re-melting of basaltic material and/or crustal assimilation episodes.

4.5 Additional considerations on spectropolarimetric observations

The spectropolarimetric results (Figs. 10, 11) cannot be interpreted in a straightforward way because, unlike for cometary dust, no sufficiently detailed multiple-scattering based physical model currently exists to relate the inferred polarimetric parameters and their wavelength dependencies to specific physical or compositional properties of densely packed regolith grains. Nevertheless, our spectropolarimetric analysis is able to differentiate between various terrain types, where different cluster assignments are likely due to variations in regolith grain properties.

Over the past decades, a large amount of polarimetric data has been acquired for a wide range of asteroids (e.g., Bendjoya et al., 2022). Since asteroids also host regolith surfaces, it is insightful to compare their polarimetric properties to those obtained in this study for the Atlas region. Typical R band values of the polarimetric parameters inferred at small phase angles for asteroids of the classes S (iron/nickel mixed with silicates), M (iron/nickel) and C (carbonaceous chondrites) are indicated in Figure 11. Asteroid of the M and C classes have compositions that are markedly different from that of the Moon, but they exhibit P_{min}, α_{min} and h values similar to those found in the Atlas region; only their typical α_{inv} values are lower by several degrees. S-class asteroids, which are compositionally most similar to the Moon, strongly differ in P_{min} and h from the lunar terrains. Furthermore, their P_{max} and α_{max} values in the V band typically correspond to 0.075 and 105°, respectively (Petrov and Kiselev, 2018), well outside the ranges encountered for the examined lunar terrains. Overall, we conclude that no asteroid class matches any of the examined lunar terrain types in all spectropolarimetric parameters, which hints at systematic structural differences between the regolith surfaces of lunar terrains and asteroids.

5 Conclusions

Remote sensing data over Atlas crater, the prime landing site of the ELM Rashid-1 mission, were investigated to decipher its geological context. CSFD measurements were conducted to estimate the crater formation age with highland materials, yielding an age of 3.82 Gy. M3 observations indicate that Atlas is a complex crater which tapped into a pluton dominated by mixed plagioclase, pyroxene, and spinel signatures. After its emplacement, the western portion of the crater was partially blanketed by the ejecta from the nearby Hercule impact at 3.71 Gy, and was later intruded by magma, causing uplift of the crater floor. Eruption of pyroclastic material from two vents in the northern and southern parts of the crater may have been contemporaneous to this intrusive episode and/or to mare basalt emplacement within the broader region. Eruption of pyroclastic deposits along two vents in the north and south of the crater may be contemporaneous to this intrusive episode, and/or to mare basalt emplacement within the greater region (although spectropolarimetry evidence suggests distinct properties and likely, distinct mode of emplacement). East of the crater, an unnamed dome formed by highly viscous flows, akin to those observed in the Gruithuisen and Mairan regions, hints at the possible presence of evolved lithologies. The thermophysical anomaly in the Diviner datasets remains unexplained and calls for further investigations of this peculiar region of high scientific potential. Atlas crater's complex volcanic history, coupled with its well-preserved record of impact processes, makes it an ideal target for addressing outstanding lunar science questions with future exploration missions (e.g., NRC, 2007; Flahaut et al., 2023).

Acknowledgements. This work is part of the framework of the Emirates Lunar Mission (ELM). The ELM is conducted by the Mohammed Bin Rashid Space Center (MBRSC), in Dubai, UAE. The ELM is funded by the ICT Fund as part of the Mars 2117 initiative. Support from the French space agency (CNES) Rashid team is much appreciated. The authors wish to express their gratitude to the LROC team for the availability of the data, and their support in imaging the ELM candidate sites throughout the entire landing site selection process and searching for the Rashid-1 impact site. This is CRPG contribution N°2883.

Open science statements

Author contributions J.F.: Conceptualization, Funding acquisition, Project administration, Investigation and analyses, Writing (original draft), and Writing (review & editing). C.W. : Conceptualization, Investigation and analyses, Writing (original draft), and Writing (review & editing). M.J., M.B., S.B.: Investigation and analyses, Writing (review & editing). E.F., S.G.E, S.A, H.A : Project administration, Writing (review & editing).

Data availability Diviner, mini-RF and LRO WAC global mosaics were downloaded from the NASA Planetary Data System (http://doi.org/https://pds-geosciences.wustl.edu/dataserv/moon.html). LROC NAC images and the LROC team DTMs are available from the LROC data node (http://doi.org/http://lroc.sese.asu.edu Kaguya TC images and DTMs are also publicly available on the JAXA's SELENE Archive (http://doi.org/https://darts.isas.jaxa.jp/planet/pdap/selene/).

Funding The work of J.F., M.J., E.F. and S.B. was funded the CNES under the “Appel à Programme de Recherche” (APR). M.B. is funded by the Physical Research Laboratory, a unit of the Department of Space, Government of India.

Competing interests The authors declare that they have no known competing financial interests or personal relationships that could have appeared to influence the work reported in this paper.

References

Almarzooqi, H., & S. AlMaeeni (2021). Rashid Rover: A Small Rover with Big Science Goals, IAC-15-E4.2.8, 72nd International Astronautical Congress (IAC), Dubai, United Arab Emirates, 25-29 October 2021.

Bandfield, J. L., R.R. Ghent, A.R. Vasavada, D.A. Paige, S.J. Lawrence & M.S. Robinson (2011). Lunar surface rock abundance and regolith fines temperatures derived from LRO Diviner Radiometer data. *Journal of Geophysical Research: Planets*, 116(E12), E00H02. http://doi.org/https://doi.org/10.1029/2011JE003866

Bandfield, J. L., Song, E., Hayne, P. O., Brand, B. D., Ghent, R. R., Vasavada, A. R., & Paige, D. A. (2014). Lunar cold spots: Granular flow features and extensive insulating materials surrounding young craters. *Icarus*, 231, 221–231. http://doi.org/https://doi.org/10.1016/j.icarus.2013.12.017

Bendjoya, P., Cellino, A., Rivet, J. P., Devogèle, M., Bagnulo, S., et al. (2022). The Calern Asteroid Polarisation Survey-An updated catalogue of asteroid polarimetric data. *Astronomy & Astrophysics*, 665, A66. http://doi.org/https://doi.org/10.1051/0004-6361/202142960

Besse, S., Sunshine, J., Staid, M., Boardman, J., Pieters, C., et al. (2013). A visible and near-infrared photometric correction for Moon Mineralogy Mapper (M3). *Icarus*, 222(1), 229–242. http://doi.org/https://doi.org/10.1016/j.icarus.2012.10.036

Besse, S., Sunshine, J.M., Gaddis, L.R., (2014). Volcanic glass signatures in spectro-scopic survey of newly proposed lunar pyroclastic deposits. *J. Geophys. Res. Planets*, 119(2), 355–372. http://doi.org/https://doi.org/10.1002/2013JE004537

Boardman, J.W., et al. (2011). Measuring moonlight: an overview of the spatial properties, lunar coverage, selenolocation, and related Level 1B products of the Moon Mineralogy Mapper. *J. Geophys. Res. Planets*, 116, E00G14. https://doi.org/10.1029/2010JE003730

Breton, S., Quantin-Nataf, C., Pan, L., Mandon, L., & Volat, M. (2022). Insight into Martian crater degradation history based on crater depth and diameter statistics. *Icarus*, 377, 114898. http://doi.org/https://doi.org/10.1016/j.icarus.2022.114898

Cahill, J.T.S., Thomson, B.J., Patterson, G.W., Bussey, D.B.J., Neish, C.D., et al. (2014). The Miniature Radio Frequency instrument's (Mini-RF) global observations of Earth's Moon. *Icarus*, 243, 173–190. http://doi.org/https://doi.org/10.1016/j.icarus.2014.07.018

Cahill, J.T.S., Hayne, P.O., Patterson, G.W., Greenhagen, B.T. (2019). The Unusual Atlas/Hercules Region of the Moon. Presented at the GSA Annual Meeting in Phoenix, Arizona, USA, 2019, p. 332001. http://doi.org/https://doi.org/10.1130/abs/2019AM-332001

Cintala, M. J., & Grieve, R. A. (1998). Scaling impact melting and crater dimensions: Implications for the lunar cratering record. *Meteoritics & Planetary Science*, 33(4), 889–912. http://doi.org/https://doi.org/10.1111/j.1945-5100.1998.tb01695.x

Clark, R.N., et al. (2011). Thermal removal from near-infrared imaging spectroscopy data of the Moon. *J. Geophys. Res. Planets*, 116, E00G16. https://doi.org/10.1029/ 2010JE003751

Czajka, E., Retherford, K., Kramer, G., Hendrix, A., Cahill, J., et al. (2023). New Insights into Aristarchus Crater with LRO LAMP Far-ultraviolet Observations. *The Planetary Science Journal*, 4(8), 137. http://doi.org/https://doi.org/10.3847/PSJ/acdee9

Dollfus, A. (1998). Lunar surface imaging polarimetry: I. Roughness and grain size. *Icarus*, 136(1), 69–103. http://doi.org/https://doi.org/10.1006/icar.1998.6008

Els, S., et al. (2021). The science system on-board the Emirates Lunar Mission's Rashid rover, EGU general assembly, abstract EGU21-12950. http://doi.org/https://doi.org/10.5194/egusphere-egu21-12950

Flahaut, J., Blanchette-Guertin, J.-F., Jilly, C., Sharma, P., Souchon, A., van Westrenen, W., Kring, D. A. (2012). Identification and characterization of science-rich landing sites for lunar lander missions using integrated remote sensing observations. *Advances in Space Research*, 50(12), 1647–1665. http://doi.org/https://doi.org/10.1016/j.asr.2012.05.020

Flahaut, J., van der Bogert, C. H., Crawford, I. A., & Vincent-Bonnieu, S. (2023). Scientific perspectives on lunar exploration in Europe. *npj Microgravity*, 9(1), 50. http://doi.org/https://doi.org/10.1038/s41526-023-00298-9

Flahaut, J., Els, S. G., Joulaud, M., Wöhler, C., Breton, S., et al. (2024). Candidate landing sites for the Emirates Lunar Mission (ELM) Rashid-1 rover. *Space Science Reviews*, 220(5), 53. https://doi.org/10.1007/s11214-024-01086-x

Fortezzo, C.M., P. D. Spudis, & Harrel, S. L. (2020), Release of the Digital Unified Global Geologic Map of the Moon At 1:5,000,000- Scale, 51st Lunar and Planetary Science Conference, Houston, TX.

Gaddis, L.R., Hawke, B.R., Robinson, M.S., & Coombs, C.R., (2000). Compositional analyses of small lunar pyroclastic deposits using Clementine multispectral data. *J. Geophys. Res. Planets*, 105(E2), 4245–4262. http://doi.org/https://doi.org/10.1029/1999JE001070

Gaddis, L.R., M.I. Staid, J.A. Tyburczy, B.R. Hawke, & Petro, N.E. (2003). Compositional analyses of lunar pyroclastic deposits. *Icarus*, 161 (2), 262–280.http://doi.org/https://doi.org/10.1016/S0019-1035(02)00036-2

Gaddis, L., B.R. Hawke, T. Giguere, S. Klem, J.O. Gustafson, S.J. Lawrence, J.D. Stopar (2012). Volcanism within floor-fractured Atlas crater. In: Lunar and Planetary Science Conference, Vol. 43.

Goidet-Devel, B., Renard, J. B., & Levasseur-Regourd, A. C. (1995). Polarization of asteroids. Synthetic curves and characteristic parameters. *Planetary and Space Science*, 43(6), 779–786. http://doi.org/https://doi.org/10.1016/0032-0633(94)00140-M

Glotch, T. D., et al. (2010), Highly silicic compositions on the Moon. *Science*, 329(5998), 1510–1513. https://doi.org/ 10.1126/science.1192148

Green, R. O., et al. (2011). The Moon Mineralogy Mapper (M3) imaging spectrometer for lunar science: instrument description, calibration, on-orbit measurements, science data calibration and on-orbit validation. *J. Geophys. Res.*, 116, 1–31, https://doi.org/10.1029/2011JE003797

Greenhagen, B. T., Lucey, P. G., Wyatt, M. B., Glotch, T. D., Allen, C. C., et al. (2010). Global silicate mineralogy of the Moon from the Diviner Lunar Radiometer. *Science*, 329(5998), 1507–1509. https://doi.org/10.1126/science.1192196.

Grolier, M. J. (1974). Geologic map of the Geminus Quadrangle of the Moon, USGS, IMAP 841. http://doi.org/https://doi.org/10.3133/i841

Hagerty, J. J., Lawrence, D. J., Hawke, B. R., Vaniman, D. T., Elphic, R. C., & Feldman, W. C. (2006). Refined thorium abundances for lunar red spots: Implications for evolved, nonmare volcanism on the Moon. *Journal of Geophysical Research: Planets*, 111(E6). http://doi.org/https://doi.org/10.1029/2005JE002592

Hapke, B. (2002). Bidirectional reflectance spectroscopy: 5. The coherent backscatter opposition effect and anisotropic scattering. *Icarus*, 157(2), 523–534. http://doi.org/https://doi.org/10.1006/icar.2002.6853

Hapke, B. (2012). *Theory of reflectance and emittance spectroscopy*. Cambridge University Press. http://doi.org/https://doi.org/10.1017/CBO9781139025683

Haruyama, J., et al. (2008). Global lunar-surface mapping experiment using the Lunar Imager/Spectrometer on SELENE. *Earth, Planets and Space*, 60(4), 243–255. http://doi.org/https://doi.org/10.1186/BF03352788

Hayne, P. O., Bandfield, J. L., Siegler, M. A., Vasavada, A. R., Ghent, R. R., et al. (2017). Global regolith thermophysical properties of the Moon from the Diviner Lunar Radiometer Experiment. *Journal of Geophysical Research: Planets*, 122(12), 2371–2400. http://doi.org/https://doi.org/10.1002/2017JE005387

Head, J.W., & Wilson, L., (1979). Alphonsus-type dark-halo craters: Morphology, morphometry, and eruption conditions. Proc. Lunar Sci. Conf., X, 525–527.

Head, J.W., & Wilson, L., (2017). Generation, ascent and eruption of magma on the Moon: new insights into source depths, magma supply, intrusions and effusive/explosive eruptions (part 2: predicted emplacement processes and observations). *Icarus*, 283, 176–223. http://doi.org/https://doi.org/10.1016/j.icarus.2016.05.031

Heather, D.J., & Dunkin, S.K. (2002). A stratigraphic study of southern Oceanus Procellarum using Clementine multispectral data. *Planetary and Space Science*, 50(14-15), 1299–1309. http://doi.org/https://doi.org/10.1016/S0032-0633(02)00124-1

Johnson, A. M., & D. P. Pollard (1973). Mechanics of growth of some laccolithic intrusions in the Henry Mountains, Utah. I. Field observations, Gilbert's model, physical properties and flow of magma. *Tectonophysics*, 18, 261–309. http://doi.org/https://doi.org/10.1016/0040-1951(73)90050-4

Joulaud, M., Flahaut, J., Allemand, P., Füri, E., Wöhler, C., et al. (2024). Investigation of the regolith thickness and boulder density at the four candidate landing sites of the Emirates Lunar Mission Rashid-1 rover. *Space Science Reviews*, 220(6), 65. http://doi.org/https://doi.org/10.1007/s11214-024-01101-1

Jozwiak, L.M., Head, J.W., Zuber, M.T., Smith, D.E., Neumann G.A. (2012). Lunar floor fractured craters. Classification, distribution, origin and implications for magmatism and shallow crustal structure. *J. Geophys. Res. Planets*, 117 (E11). https://doi.org/10.1029/2012JE004134

Jozwiak, L.M., J.W. Head, & L. Wilson (2015). Lunar floor-fractured craters as magmatic intrusions. Geometry, modes of emplacement, associated tectonic and volcanic features, and implications for gravity anomalies. *Icarus*, 248, 424–447. http://doi.org/https://doi.org/10.1016/j.icarus.2014.10.052

Keske, A. L., Clarke, A. B., & Robinson, M. S. (2020). On the eruptive origins of lunar localized pyroclastic deposits. *Earth and Planetary Science Letters*, 547, 116426, https://doi.org/10.1016/j.epsl.2020.11642

Kiselev, N., Rosenbush, V., Levasseur-Regourd, A.-C., Kolokolova, L. (2015). Comets. In: L. Kolokolova, J. Hough, A. Levasseur-Regourd (Eds.), *Polarimetry of Stars and Planetary Systems*, Cambridge University Press, p. 379.

Kokaly, R. F., Clark, R. N., Swayze, G. A., Livo, K. E., Hoefen, T. M., et al. (2017). USGS spectral library version 7 (No. 1035). US Geological Survey. http://doi.org/https://doi.org/10.3133/ds1035

Lawrence, D. J., W. C. Feldman, B. L. Barraclough, A. B. Binder, R. C. Elphic, S. Maurice, & D. R. Thomsen (1998). Global elemental maps of the Moon: The Lunar Prospector Gamma-Ray Spectrometer. *Science*, 284, 1484–1489. http://doi.org/https://doi.org/10.1016/S0168-9002(98)00934-6

Losiak, A., Wilhelms, D. E., Byrne, C. J., Thaisen, K. G., Weider, S. Z., et al. (2009). A new lunar impact crater database. In 40th Annual lunar and planetary science conference, p. 1532.

Lucey, P.G., Blewett, D.T. & Jolliff, B.L. (2000). Lunar iron and titanium abundance algorithms based on final processing of Clementine ultraviolet-visible images. *Journal of Geophysical Research: Planets*, 105(E8), 20297–20305. http://doi.org/https://doi.org/10.1029/1999JE001117

Lucey, P. G., Greenhagen, B., Donaldson Hanna, K., Bowles, N., Flom, A., & Paige, D. A. (2021). Christiansen feature map from the lunar reconnaissance orbiter diviner lunar radiometer experiment: Improved corrections and derived mineralogy. *Journal of Geophysical Research: Planets*, 126(6), e2020JE006777. http://doi.org/https://doi.org/10.1029/2020JE006777

Marsland, S. (2015). *Machine Learning: An Algorithmic Perspective* (2nd ed.). CRC Press. http://doi.org/https://doi.org/10.1201/b17476

Martinot, M., Besse, S., Flahaut, J., Quantin-Nataf, C., Lozac'h, L., & Van Westrenen, W. (2018). Mineralogical diversity and geology of Humboldt crater derived using Moon Mineralogy Mapper data. *Journal of Geophysical Research: Planets*, 123(2), 612–629. http://doi.org/https://doi.org/10.1002/2017JE005435

Michael, G.G., & Neukum, G. (2010). Planetary surface dating from crater size-frequency distribution measurements: Partial resurfacing events and statistical age uncertainty. *Earth and Planetary Science Letters*, 294 (3-4), 223–229. http://doi.org/https://doi.org/10.1016/j.epsl.2009.12.041

Michael, G. G., Kneissl, T., & Neesemann, A. (2016). Planetary surface dating from crater size-frequency distribution measurements: Poisson timing analysis. *Icarus*, 277, 279–285. http://doi.org/https://doi.org/10.1016/j.icarus.2016.05.019

Misra, D., Bhatt, M., Hess, M., & Wöhler, C. (2026). An integrated framework for global detection and quantification of lunar pyroclastic deposits. *Planetary Science Journal*, 7, 24. http://doi.org/https://doi.org/10.3847/PSJ/ae317c

Mustard, J. F., Pieters, C. M., Isaacson, P. J., Head, J. W., Besse, S., et al. (2011). Compositional diversity and geologic insights of the Aristarchus crater from Moon Mineralogy Mapper data. *Journal of Geophysical Research: Planets*, 116(E6). http://doi.org/https://doi.org/10.1029/2010JE003726

Neal, C. R., & Taylor, L. A. (1989). Lunar granite petrogenesis and the process of silicate liquid immiscibility: the barium problem. In *Moon in Transition: Apollo 14, KREEP, and Evolved Lunar Rocks*, pp. 89–93.

Neukum, G., Ivanov, B. A., & Hartmann, W. K. (2001). Cratering records in the inner solar system in relation to the lunar reference system. *Space Science Reviews*, 96(1), 55–86. http://doi.org/https://doi.org/10.1023/A:1011989004263

NRC (National Research Council) (2007). The Scientific Context for Exploration of the Moon. Washington, DC: The National Academies Press. http://doi.org/https://doi.org/10.17226/11954

Pathak, S., Dagar, A.K., Bhattacharya, S., Moitra, H., Chauhan, M., Gupta, S. (2021). Geological insights into lunar floor-fractured crater Atlas. *Icarus*, 360, 114374. http://doi.org/https://doi.org/10.1016/j.icarus.2021.114374

Petrov, D., & Kiselev, N. (2018). Computer simulation of position and maximum of linear polarization of asteroids. *Journal of Quantitative Spectroscopy and Radiative Transfer*, 204, 88–93. http://doi.org/https://doi.org/10.1016/j.jqsrt.2017.09.003

Pieters, C. M., Hiroi, T., Pratt, S. F., & Patterson, B. (2004). Reflectance Experiment Laboratory (RELAB) Description and User's Manual.

Pieters, C.M., et al. (2009). The Moon mineralogy mapper (M3) on chandrayaan-1. *Science*, 96, 1–6.

Pike, R. J. (1980), Geometric interpretation of lunar craters, U.S. Geol. Surv. Prof. Pap., 1046- C, C1–C77.

Prasad, B., & Das, H. S. (2024). Unveiling the properties of asteroids: linking photopolarimetry to spectral classification. *Monthly Notices of the Royal Astronomical Society*, 532(1), 22–31. http://doi.org/https://doi.org/10.1093/mnras/stae1409

Robbins, S. J., Riggs, J. D., Weaver, B. P., Bierhaus, E. B., Chapman, C. R., et al. (2018). Revised recommended methods for analyzing crater size-frequency distributions. *Meteoritics & Planetary Science*, 53(4), 891–931. http://doi.org/https://doi.org/10.1111/maps.12990

Robinson, M.S., Brylow, S.M., Tschimmel, M., Humm, D., Lawrence, S.J., et al. (2010). Lunar Reconnaissance Orbiter Camera (LROC) Instrument Overview. *Space Sci Rev*, 150, 81–124. https://doi.org/10.1007/s11214-010-9634-2

Rutherford, M. J., Hess, P. C., Ryerson, F. J., Campbell, H. W., & Dick, P. A. (1976). The chemistry, origin and petrogenetic implications of lunar granite and monzonite. In *Lunar and Planetary Science Conference Proceedings*, Vol. 7, pp. 1723-1740.

Schnuriger, N., Flahaut, J., Martinot, M., & Chevrel, S. D. (2020). Long-lived volcanism expressed through mare infilling, domes and IMPs in the Arago region of the Moon. *Planetary and Space Science*, 185, 104901. http://doi.org/https://doi.org/10.1016/j.pss.2020.104901

Schultz, P.H. (1976). Floor-fractured lunar craters. *Earth Moon Planet*, 15(3), 241–273. http://doi.org/https://doi.org/10.1007/BF00562240

Seddio, S. M., Jolliff, B. L., Korotev, R. L., & Zeigler, R. A. (2013). Petrology and geochemistry of lunar granite 12032, 366-19 and implications for lunar granite petrogenesis. *American Mineralogist*, 98(10), 1697–1713. http://doi.org/https://doi.org/10.2138/am.2013.4330

Shkuratov, Y. G., Opanasenko, N. V., & Kreslavsky, M. A. (1992). Polarimetric and photometric properties of the moon: Telescopic observations and laboratory simulations: 1. The negative polarization. *Icarus*, 95(2), 283–299. http://doi.org/https://doi.org/10.1016/0019-1035(92)90044-8

Shkuratov, Y. G., & Opanasenko, N. V. (1992). Polarimetric and photometric properties of the moon: Telescope observation and laboratory simulation: 2. The positive polarization. *Icarus*, 99(2), 468–484. http://doi.org/https://doi.org/10.1016/0019-1035(92)90161-Y

Shkuratov, Y., Kaydash, V., Gerasimenko, S., Opanasenko, N., Velikodsky, Y., et al. (2010). Probable swirls detected as photometric anomalies in Oceanus Procellarum. *Icarus*, 208(1), 20–30. http://doi.org/https://doi.org/10.1016/j.icarus.2010.01.028

Siegler, M. A., Feng, J., Lehman-Franco, K., Andrews-Hanna, J. C., Economos, R. C., et al. (2023). Remote detection of a lunar granitic batholith at Compton–Belkovich. *Nature*, 620(7972), 116–121. http://doi.org/https://doi.org/10.1038/s41586-023-06183-5

Smith, D. E., et al. (2017). Summary of the results from the Lunar Orbiter Laser Altimeter after seven years in lunar orbit. *Icarus*, 283, 70–91. http://doi.org/https://doi.org/10.1016/j.icarus.2016.06.006

Wichman, R. W., & Schultz, P. H. (1995). Floor-fractured craters in Mare Smythii and west of Oceanus Procellarum: Implications of crater modification by viscous relaxation and igneous intrusion models. *Journal of Geophysical Research: Planets*, 100(E10), 21201–21218. http://doi.org/https://doi.org/10.1029/95JE02297

Wieczorek, M. A., Neumann, G. A., Nimmo, F., Kiefer, W. S., Taylor, G. J., et al. (2013). The crust of the Moon as seen by GRAIL. *Science*, 339(6120), 671–675. http://doi.org/https://doi.org/10.1126/science.1231530

Wilson, L., & Head, J. W. (2003). Lunar Gruithuisen and Mairan domes: Rheology and mode of emplacement. *Journal of Geophysical Research: Planets*, 108(E2). http://doi.org/https://doi.org/10.1029/2002JE001909

Wilson, L., Head, J.W., (2017). Generation, ascent and eruption of magma on the Moon: new insights into source depths, magma supply, intrusions and effusive/explosive eruptions (part 1: theory). *Icarus*, 283, 146–175. http://doi.org/https://doi.org/10.1016/j.icarus.2016.05.031

Wöhler, C., Lena, R., & Phillips, J. (2007). Formation of lunar mare domes along crustal fractures: Rheologic conditions, dimensions of feeder dikes, and the role of magma evolution. *Icarus*, 189(2), 279–307. http://doi.org/https://doi.org/10.1016/j.icarus.2007.01.011

Wöhler, C., Grumpe, A., Berezhnoy, A., Bhatt, M. U., & Mall, U. (2014). Integrated topographic, photometric and spectral analysis of the lunar surface: Application to impact melt flows and ponds. *Icarus*, 235, 86–122. http://doi.org/https://doi.org/10.1016/j.icarus.2014.03.010

Wöhler, C., et al. (2017). Time-of-day–dependent global distribution of lunar surficial water/hydroxyl. *Sci. Adv.*, 3, e1701286. http://doi.org/https://doi.org/10.1126/sciadv.1701286

Wöhler, C., Arnaut, M., & Bhatt, M. (2024). Multiband spectropolarimetry of lunar maria, pyroclastics, fresh craters, and swirl materials. *The Astronomical Journal*, 167(5), 187. http://doi.org/https://doi.org/10.3847/1538-3881/ad2f2f

Wohlfarth, K., et al. (2023). An advanced thermal roughness model for airless planetary bodies - Implications for global variations of lunar hydration and mineralogical mapping of Mercury with the MERTIS spectrometer. *A&A*, 674, A69. http://doi.org/https://doi.org/10.1051/0004-6361/202245343

Zubko, E., Videen, G., Arnold, J. A., MacCall, B., Weinberger, A. J., Kim, S. S. (2020). On the Small Contribution of Supermicron Dust Particles to Light Scattering by Comets. *Astrophys. J.*, 895, 110. http://doi.org/https://doi.org/10.3847/1538-4357/ab8ae4

Supplemental figures

From: Flahaut, J., et al. (2026). Geology of Atlas crater, the prime landing site of the Emirates Lunar Mission Rashid-1 rover. *Planetary Research*, **1**(1), 274. https://doi.org/10.53480/4e7a-4y94

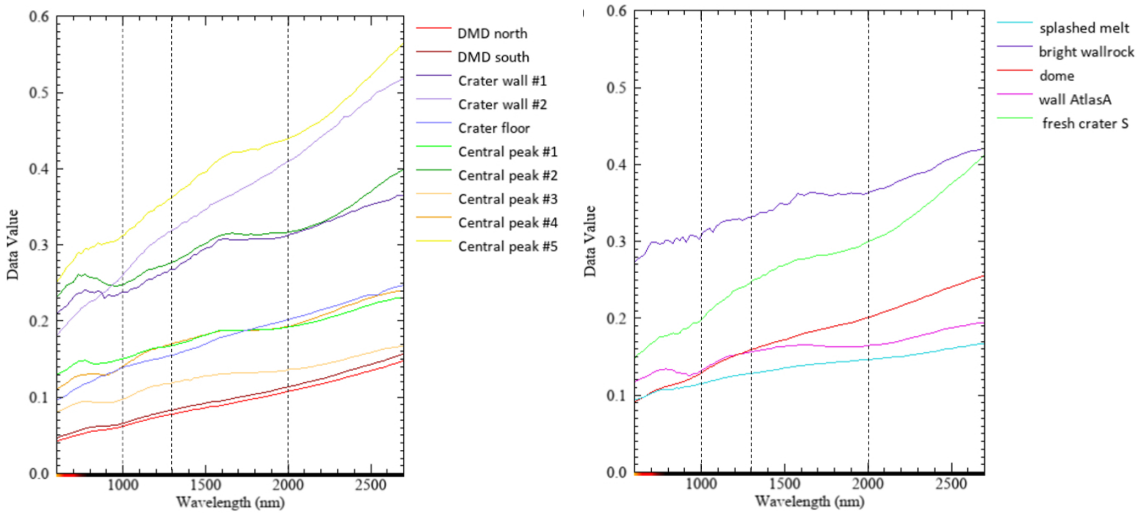

(a) **(b)**

Figure S1 | M3 spectra collected over regions of interest within Atlas crater (a) and in the surroundings of the unnamed dome (b). Vertical bars were added at 1000, 1300 and 2000 nm to help locate the main absorption bands of pyroxenes and plagioclase feldspars. Corresponding continuum-removed spectra are presented in Figure 8.

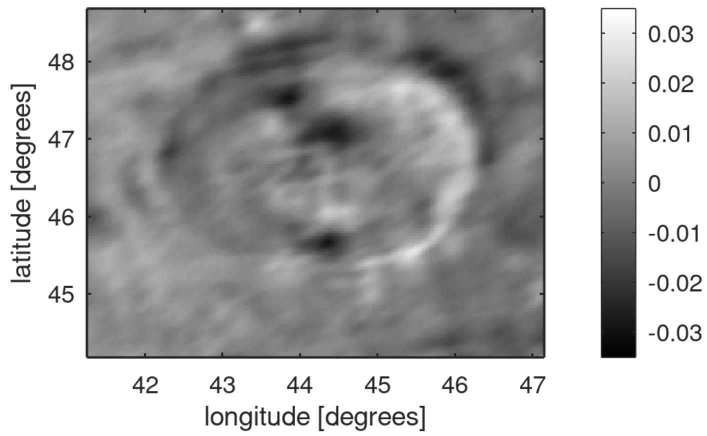

Figure S2 | Phase ratio image of Atlas crater obtained by dividing the I-band intensity data at 4° phase angle by those at 9° phase angle, depicted in decadal logarithmic scale. Due to the lack of absolute reflectance calibration, the phase ratios were normalized to a mean value of 1.